UC Berkeley
UC Berkeley Previously Published Works

Title
Components and Tidal Modulation of the Wave Field in a Semi-enclosed Shallow Bay

Permalink
https://escholarship.org/uc/item/7154w042

Journal
Estuaries and Coasts, 46(3)

ISSN
1559-2723

Authors

WinklerPrins, Lukas
Largier, John L
Vila-Concejo, Ana
et al.

Publication Date
2023-05-01

DOI
10.1007/s12237-022-01154-x

Copyright Information

Peer reviewed

Components and Tidal Modulation of the Wave Field in a Semi-enclosed Shallow Bay

Lukas WinklerPrins[1] · John L. Largier[2] · Ana Vila-Concejo[3] · Shari L. Gallop[4,5] · Thomas E. Fellowes[3] · Maryam Rahbani[3,6]

Abstract

The wave fields of coastal bays are comprised of waves generated by far-off storms that enter the bay to combine with waves generated locally by winds inside the bay and regionally outside the bay. In any given location, the resultant wave field varies spatially and temporally, and affects coastal features, such as beaches in estuaries and bays (BEBs). However, wave fields in enclosed bays with tidal shoals are poorly studied, limiting the efficacy of coastal protection and restoration projects in these systems, a critical focus in light of ongoing sea level rise. Here we present observations of the wave field in Tomales Bay, a 20-km-long, narrow, semi-enclosed embayment on the wave-dominated coast of Northern California (USA) with a spring-tide range of 2.5 m. We deployed pressure sensors near several beaches along the linear axis of the bay. Low-frequency waves ($4 * 10^{-2} - 2.5 * 10^{-1}$ Hz or 4–25-s period) were not observed further than 4 km of the mouth, delineating the "outer bay" region, where remotely generated swell and regionally generated wind waves could dominate. The wave spectrum of the landward "inner bay" was dominated by fetch-limited waves generated within the bay with frequency $\geq 2.5 * 10^{-1}$ Hz. The energy of both ocean waves and locally generated wind waves across all sites were controlled by the tide, but the former by changes in attenuation and the latter likely by modulation of wave generation. Wave energies were low at low tide and high at high tide, but high-frequency wind wave energy was increased during ebb tides while lower-frequency swell energy was reduced during ebb tides, suggesting different mechanisms of tidal influences. Thus, in addition to fluctuations in winds and the presence of ocean waves, tides exert a strong control on the wave energy spectra at coastal features in mesotidal regions. In general, events that may be impactful for BEB morphology are expected to occur when waves due to high winds or high-swell event arrive during high-tide periods. However, no such events were observed during our study and questions remain as to how rarely such events occur across the bay.

Keywords Sheltered beach · Low-energy beach · Shallow-water waves · Spectral analysis · Wind waves

---

✉ Lukas WinklerPrins
lukas_wp@berkeley.edu

1 Civil & Environmental Engineering, University of California, Berkeley, Berkeley, USA

2 Bodega Marine Laboratory, University of California, Davis, Bodega Bay, USA

3 Geocoastal Research Group, The University of Sydney, Sydney, Australia

4 School of Science, University of Waikato, Tauranga, New Zealand

5 Environmental Research Institute, University of Waikato, Hamilton, New Zealand

6 Department of Marine Science and Technology, University of Hormozgan, Bandar Abbas, Iran

Introduction

The dominance of different nearshore waves—the drivers of wear and morphologic change on built and natural elements, respectively—along the coastlines of estuaries and bays around the world, remain poorly understood and highly specific to the geographic conditions of the site. Inside bays, due to the persistent lack of ocean swell energy, mechanisms such as periodic local storm events (Gallop et al. 2020; Leonardi et al. 2016) or hydrodynamic processes (such as tidal currents, surge, or infragravity waves, Vila-Concejo et al. (2020)) may be larger contributors to nearshore dynamics than on open coast coastal systems. Still, features such as beaches in estuaries and bays (BEBs) and mudflat-marsh complexes are products of "low-energy" wave fields inside

sheltered embayments (Fellowes et al. 2021; Lacy and MacVean 2016; Jackson et al. 2002). In shallow embayments especially, waves that drive morphologic change to the coastal edge may only occur at particular water levels, based on tidal stage or river outflow, as in Eliot et al. (2006) and Fagherazzi and Wiberg (2009).

The wave field inside an embayment is a combination of both locally generated waves and those that enter from the open ocean. Local wave production inside bays is often limited by fetch (Jackson et al. 2002), but may also be limited by depth in shallow systems (Young and Verhagen 1996). Longer-period ocean-originating waves are generally dissipated as they enter the mouth(s) of the embayment. Observational wave data of finite-depth, fetch-limited systems are rare (Fagherazzi and Wiberg 2009). As waves of all frequencies travel through an embayment, they are subject to a variety of forces that modify the water surface spectra, including refraction, diffraction, dissipation by bottom friction, and interactions with currents (Davidson et al. 2008). The effects of bottom friction and bathymetric features may drive nonlinear exchanges of energy between waves of different frequencies (Zhu et al. 2020; Matsuba et al. 2021) or interact with tidal currents (Davidson et al. 2008), introducing tidal timescales relevant to the wave energy delivered to the shore.

Literature that decomposes wave dynamics by frequency to address the potential impacts of waves on shorelines across space and time is rare. Additionally, discriminating between wave-generating and wave-attenuation processes from within versus outside an embayment remains understudied (after Jackson et al. (2002)). Differences in wave properties may be used to predict properties about morphologic dynamics of beaches (Rahbani et al. 2022) or marshes (Marani et al. 2011), but the aforementioned scarcity in detailed wave data inside bays makes this connection difficult to build. In this paper, we use surface wave spectra to quantify the wave fields at pressure sensors installed near beaches inside Tomales Bay, California, whose linear geometry is in-line with the dominant wind and swell direction and allows for a unique opportunity to relate changes in the wave field to linear distance from the mouth and along the fetch. We delineate the drivers of wave motion across three ranges of frequencies, corresponding to locally generated wind waves, ocean swell, and infragravity motions. In addition to sharing more data about in-bay wave spectra, we thus address three objectives: (1) to investigate the temporal dynamics and spatial dominance of wind chop energy across the bay; (2) to determine how far lower-frequency waves penetrate past the mouth; and (3) to examine how tidal stage affects the combined wave field. Through these goals, we improve conceptual models for how wave fields in bays are developed and vary spatially and temporally, and discuss the potential morphologic implications for BEBs.

Regional Context

Tomales Bay is a long, shallow embayment on the northern California coast, USA (Fig. 1), approximately 20 km long,

Fig. 1 Locations of instruments (S1-S4) installed in Tomales Bay (**b**, **c**) as well as some geographic reference points. Only the outer bay is visible in (**c**). Context in California given in (**a**)
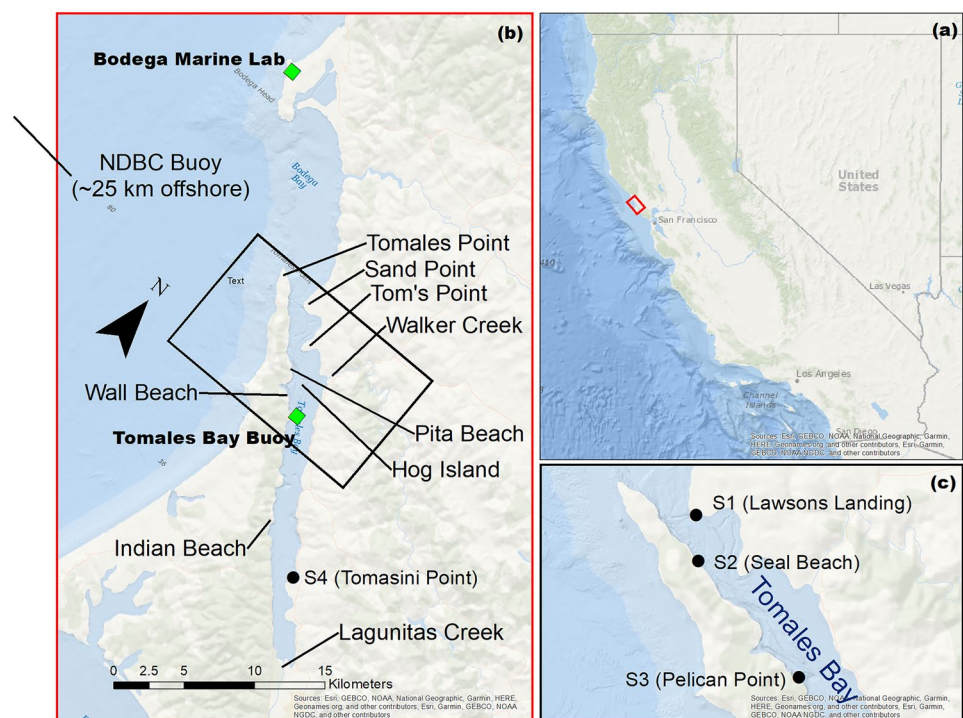
2 km wide, and only 6 m deep on average, although a channel of up to 18 m deep persists near the mouth (Anima et al. 2008). The bay is a nearly linear rift valley of the San Andreas Fault, which runs the length of the bay, delineating the boundary between the Pacific and North American plates, aligned approximately 320° from north.

Weather patterns in the area follow a Mediterranean climate with a dry summer and fall and wet winter and spring. Our study period fell in the dry months, and September–November 2019 had no rain events. Winds during this storm-free period were dominated by a daily sea breeze of afternoon onshore winds and evening or early-morning calm. The summer wave climate is mostly northwest wind swell (commonly 12-s period, H_S values offshore of 1–2 m), with some long-period south or southwesterly swells (commonly 14-s period, H_S values offshore of 0.5–0.8 m) arriving from the south Pacific. In the winter, storms in the north Pacific deliver larger and longer-period waves from the northwest.

Inside Tomales Bay, there are many sandy beaches which are "low-energy," in line with the characterization by Jackson et al. (2002); they are subject to small wave heights and rare local storm events in the rainy season. These beaches inside Tomales Bay are generally small (< 300 m in length, typically < 15 m in width) pocket beaches between rocky outcrops or headlands. Sediment inputs include small, steep watersheds on both sides of the bay, and Lagunitas Creek (at the head of the Bay) and Walker Creek (Fig. 1) which contribute mostly fine sand and coarse silt (Anima et al. 2008).

Tides in Tomales Bay are semi-diurnal with 1.76 m between mean higher-high and mean lower-low water metrics (NOAA 2020). The data recorded during our study period reflected that the tidal range does not vary with distance from the mouth, but there was an approximately 30-min lag time in water levels between our northmost and southmost sensors, which were 14.8 km apart.

Methods

Sensor Deployment

RBRsolo[3] D sensors recording pressure continuously at 2 Hz were installed at Lawsons Landing, Seal Beach, Pelican Point,

and Tomasini Point (locations hereafter named S1, S2, S3, and S4 respectively, going from closer to the mouth to more interior in the bay) (Fig. 1). S4 was deployed on 29 August, the other three on 27 September 2019. S1, S2, and S4 were recovered on 24 November 2019, and S3 was recovered on 11 December 2019. S1 was zip-tied to the southwestern-most piling on the Lawsons Landing Pier, whereas the other three were zip-tied to screw anchors installed in the bay floor. More data on sensor locations are in Table 1. Throughout the paper, the "study period" refers to 27 September – 24 November 2019.

Weather and Buoy Data

The Bodega Marine Lab (BML) maintains a meteorological station and suite of sensors. For our analysis, we used (non-gust) wind speed and direction data collected 10 m above ground surface at BML. We also used water salinity and temperature data collected on the BML Tomales Bay Buoy, inside the bay near Pelican Point (Fig. 1). Wave data are from Buoy 46013, managed by the National Data Buoy Center (NDBC 2020). We used significant wave height (H_S), peak wave period (T_p) and dominant wave direction data for this buoy, offshore of Bodega Head, approximately 25 km northwest of the mouth of Tomales Bay. All data were logged hourly, with details included in Table 2.

Data Processing and Calculations

Raw pressure data from the RBR sensors, $p_r(t)$, were converted to water depth, $h(t)$, by subtracting barometric pressure, $p_b(t)$, from the nearest hour and then converted to hydrostatic depth $h(t)$ using Eq. 1 (where z_I is the instrument height above bed and g is gravitational acceleration).

$$h(t) = \frac{p_r(t) - p_b(t)}{\rho(t)g} + z_I \tag{1}$$

Water density values, $\rho(t)$, were calculated following Millero et al. (1980) using water temperature and salinity data from the BML Tomales Bay Buoy.

We calculated and analyze spectral metrics of the pressure timeseries data every 15 mins, with each centered 15-min data point representing an six-ensemble average of depth

Table 1 Distance from the mouth was measured along the main axis of the bay from Tomales Point (Fig. 1). Depths along the fetch are mean depths of 4 m bathymetry collected by Anima et al. (2008), using MLLW as vertical datum

Sensor	Dist. to Tomales Pt.	Avg. Depth Along Fetch from Tomales Pt.	Elev. Above Bed
S1	2.3 km	n/a (protected by Sand Point)	460 cm
S2	3.4 km	6.31 m	14 cm
S3	8.0 km	8.25 m	20 cm
S4	17.4 km	6.38 m	5 cm

Table 2 Sources for wind and offshore wave data near Tomales Bay. Wave and wind directions use nautical convention

Parameter	Collection Agency	Location	Regularity
Wind Speed (non-gust)	BML	Bodega Head	On The Hour
Wind Direction	BML	Bodega Head	On The Hour
Barometric Pressure	BML	Bodega Head	On The Hour
Water Salinity	BML	Tomales Bay Buoy	On The Hour
Water Temperature	BML	Tomales Bay Buoy	On The Hour
Offshore H_S	NOAA	NDBC Buoy 46013	Hourly at :40
Offshore T_p	NOAA	NDBC Buoy 46013	Hourly at :40
Offshore Wave Direction	NOAA	NDBC Buoy 46013	Hourly at :40

spectrum $S_D(f)$, calculated from detrended 10-min overlapping windows with a Hanning filter applied. The sensor at S4 went dry at very low tides during the study period; when any window contained an average depth of < 1 cm, the ensemble metrics were not calculated.

Therefore in order to avoid making calculations based off sensor noise in these scenarios, we used a high-frequency cutoff of

$$f = \sqrt{\frac{g}{4\pi(h - z_I)}} \tag{2}$$

following Foster-Martinez et al. (2018), where z_I is the elevation of the instrument, as the upper limit of frequency that penetrates to the depth of the sensor, based on linear wave theory. As a rough estimate of the worst case (deepest sensor, S1), motions with frequencies higher than 0.625 Hz (1.6 s) are not well-captured at highest tides and not incorporated into spectral metrics. Spectral energy density values for frequencies above 0.625 Hz were less than 1% of the cumulative total for every ensemble at every sensor.

The pressure sensors were bottom-mounted and thus depth below the surface varies tidally. The ability of the sensor to detect pressure changes due to changes in surface elevation heights varies with depth below surface. Thus, we transformed each 10-min depth spectrum $S_d(f)$ into a surface-height spectrum $S_\eta(f)$ via

$$S_\eta(f) = \left[\frac{N(f)}{K_p(f)}\right]^2 S_d(f) \tag{3}$$

where N is an empirical correction factor, set equal to 1 (per Bishop and Donelan (1987), Eq. 8), and $K_p(f)$ is the pressure response factor, used to adjust for small waves causing pressure variations that may not penetrate deeply enough to reach the sensors. This method is supported by Ellis et al. (2006) and Jones and Monismith (2007). The spectral curves presented throughout the paper are the variance-preserving spectra so as to more easily visualize the frequency ranges that account for the most energetic contributions to the shore.

Each ensemble was classified as either "Low Tide," "High Tide," "Flooding," or "Ebbing," based on the slope of the depth record and proximity to peaks and troughs in the depth timeseries (i.e., the tidal signal). Category delineations were adjusted to result in similar counts of ensembles placed in each category over the entire study period, regardless of wind and swell conditions.

Significant wave height values H_S are H_{m_0} values, found via

$$H_S = 4\sqrt{m_0} \tag{4}$$

where m_0 is the 0th spectral moment. To break H_S into subcomponents by frequency ($H_{S, \text{wind}}$, $H_{S, \text{swell}}$, and $H_{S, \text{IGW}}$), we integrated within specified frequency bands that are detailed in "Frequency Band Classification", similar to Hughes et al. (2014).

We compared our calculated H_S values to those predicted by the nondimensionalized fetch-limited finite-depth wave development equations in Young and Verhagen (1996), by using the wind speed at 10 m above ground as measured at Bodega Marine Lab, and transformed predicted wave energy E into wave heights via $H_S^2 = \sqrt{(\frac{16E}{\rho g})}$.

Using the dispersion relationship $f^2 = gk \tanh(kh)$, we found the wavenumber (k) for a given frequency (f) and used that to calculate phase speed C_p and group speed C_g of waves in water depth h.

$$C_p = \sqrt{\frac{g}{k} \tanh(kh)} \tag{5}$$

$$C_g = C_p * (\frac{1}{2} + \frac{kh}{\sinh(2kh)}) \tag{6}$$

We calculated bottom velocities and shear stresses, u_b and τ_b respectively, following Wiberg and Sherwood (2008) for consideration of onset of sediment motion where h is water depth (m) and k is the wavenumber (1/m).

$$u_b = \frac{H_S \pi}{T \sinh kh} \tag{7}$$

$$\tau_b = \frac{\rho f_w}{2} u_b^2 \qquad (8)$$

We used $f_w = 2Re_w^{-0.5}$ as the wave friction factor (per Nielsen (1992)) which assumes a laminar wave boundary layer, as all measurements (except for 2% of those at S4) met the $Re_w < 3 * 10^5$ criterion.

We then calculated the Shields Parameter τ_* using Eq. 9 to evaluate the onset of granular motion when $\tau_* > 0.047$ under the waves per Madsen and Grant (1975).

$$\tau_* = \frac{\tau_b}{(\rho_s - \rho)gD_{50}} \qquad (9)$$

Where ρ_s is the sediment density, ρ is water density, and D_{50} is the median grain size.

Frequency Band Classification

We established cutoffs in frequency to delineate types of wave, distinguishing waves generated inside the bay by local winds from waves generated outside the bay (comprised of remotely generated swell waves and regionally generated low-frequency wind waves that propagate into the bay). In the following we will use "swell waves" to refer to both true ocean swell and low-frequency wind waves generated outside the bay by strong and spatially extensive regional winds along the coast of California (e.g., McPhee-Shaw et al. 2011). Infragravity waves (IGW) may be generated offshore or through energy transferred from swell waves as they shoal, as discussed in Bertin et al. (2018).

Assuming that waves generated by local winds in Tomales Bay are fetch-limited and in finite-depth, we used equations 3 and 6 from Young and Verhagen (1996) to suggest a lower bound frequency f_p for waves generated by winds in the bay. We used the longest fetch in the bay (17.4 km from Tomales Point to S4, parallel to the major axis of bay) and the highest sustained wind speed observed (25 m/s on September 28). Over this distance, the average depth was 6.4 m MLLW, according to Anima et al. (2008). The Young and Verhagen (1996) equations predict $f_p = 0.252$ Hz or $T_p = 3.98$ s. Given this estimate, and that we observed wave energy at frequencies as low as 0.29 Hz (3.44 s) at S4, which does not receive any swell wave energy, given its long distance from the mouth, we chose a 4-s period as the cutoff to classify locally generated wind waves. Thus, $H_{S,\text{wind}}$ values are derived by finding m_0 by integrating the spectral curve for all frequencies between 0.25 Hz and the high-frequency cutoff value.

Waves with frequencies lower than 0.25 Hz (4 s) but higher than 0.04 Hz (25 s) are classified as swell (with their $H_{S,\text{swell}}$ value found by integrating between the two frequencies). The cutoff separating swell from infragravity is based on Okihiro and Guza (1995) and Bertin et al. (2018). The maximum

dominant wave period measured during our study period at NDBC Buoy 46013 was 19 s (0.0526 Hz), within our swell cutoff. We applied a low-frequency limit of IGW motions at 0.003 Hz (300 s) due to its agreement with Okihiro and Guza (1995); Williams and Stacey (2016), and Beach and Sternberg (1992). $H_{S,\text{IGW}}$ values were calculated by integrating the spectral curve between 0.04 and 0.003 Hz.

Sediment Grain Size

Surface sediment samples (3 cm deep) were collected by hand during initial sensor installation in June 2019 at the beaches near S1, S2, and S3, with three samples per site chosen at random from the upper beach. The samples were dried in an oven at 32 °C overnight and then sieved using Hogentogler meshes selected to focus on fine-to-coarse sand to develop grain size distributions by mass. Mesh sizes used were 16, 11.2, 8, 5.6, 4, 2.8, 2, 1.4, 1, 0.71, 0.5, 0.355, 0.25, 0.18, 0.125, 0.09, and 0.063 mm, which are approximately evenly spaced increments in phi space (Wentworth 1922). Sediment that passed through the smallest 0.063 mm mesh was considered "fine" and accounted for less than 1% of the total sample weight in any sample. Values presented are the mean of the three D50 values (from the three samples). There were no sediment samples taken at the beach at S4.

Results

Overview of Observed Wave Field

The most common wave direction at the offshore buoy was 313°, aligned with the regional shoreline (Fig. 1), and the distribution of directions was between 295 and 320° for 78% of the study period, only deviating significantly during conditions with $H_S < 1.5$ m. Wave height H_S at the offshore buoy had mean of 1.9 m and was below 1.0 m for 13% of the study period. The dominant wave period T_p had a mean of 11.6 s and was less than 8 s for 11% of the study period. Modal wave conditions were punctuated by low-frequency swell events with $H_S > 2$ m. The buoy recorded a maximum H_S of 4.33 m and maximum period T_p of 19 s during our study. As expected for waves generated remotely, T_p at the buoy decreased over the course of swell events. During swell events with wave heights > 2.5 m and dominant wave periods > 12 s at the buoy, an increase in wave energy across a broad range of lower frequencies was observed at the sensors (i.e., infragravity waves). In addition to swell events, higher frequency wave events occurred during wind events (i.e., regionally generated wind waves) with wave heights of 2 m and $T_p < 8$ s. Together these swell waves and regional wind waves comprise the ocean waves incident on the mouth of Tomales Bay.

Between synoptic-scale wind events, which were observed to contribute energy to a wide range of frequencies, a typical daily sea breeze pattern was observed with calm mornings (wind < 6 m/s) and moderately strong winds in the late afternoon and evening (typically 8–10 m/s). Winds were mostly northwesterly, along the axis of the Bay, with directions between 280 and 360° N for 56% of the study period and 318° N being the most common direction. At times, southeasterly winds were observed, also aligned with the axis of the Bay (winds between 90 and 140° N were observed for 23% of the study period). The strongest winds, however, were from the northwest: 72% of winds > 20 m/s were winds between 280 and 360° N.

Across all frequencies, the time-averaged spectral power level was less than $1 * 10^{-15}$ m²/Hz at all four sensors. However, the wave field was punctuated by events with spectral power levels above this background, and occasional events when spectral power exceeded $1 * 10^{-8}$ m²/Hz at specific frequencies (henceforth referred to as "high-energy events"). These events are driven by particular combinations of tide,

wind, and swell conditions, further documented in "Temporal Variability in Wave Field". Our wave energy density levels are very small compared to those in other studies, reflecting the low-energy nature of the beaches in Tomales Bay: as a point of comparison, the highest-energy events (e.g., the wind event in Fig. 2) have spectral energy density of $\mathcal{O}(10^{-6})$ m²/Hz, whereas the minimum spectral density observed during a wave study by Matsuba et al. (2021) in an ocean-exposed bay in Japan was $\mathcal{O}(10^{-4})$ m²/Hz.

Spectra from S1 (Lawsons Landing, closest to the mouth) always displayed negligibly small energy in the high-frequency range, likely due to the sensor being deployed on a south-facing beach, sheltered from ocean waves and lacking a fetch longer than 3 km in any direction. Swell- and infragravity-frequency energy levels, unlike patterns observed at S2 discussed later in the paper, were typically high just before and after low tide conditions. The sensor location at S1 was in the deepest water (Table 1) and subject to strong tidal currents due to its position in a deep channel near the mouth. Due to the different orientation, wave timing, and impact of tidal currents at S1, we chose not to

Fig. 2 Wave energy density spectra at S4 with water depth (**a**) and wind conditions at BML (**b**), plotted over time with two afternoon/evening sea breeze events evident. Magenta lines are the cutoff frequencies between $H_{S,wind}$, $H_{S,swell}$, and $H_{S,IGW}$. Increased wind-wave energy is evident during periods of high winds
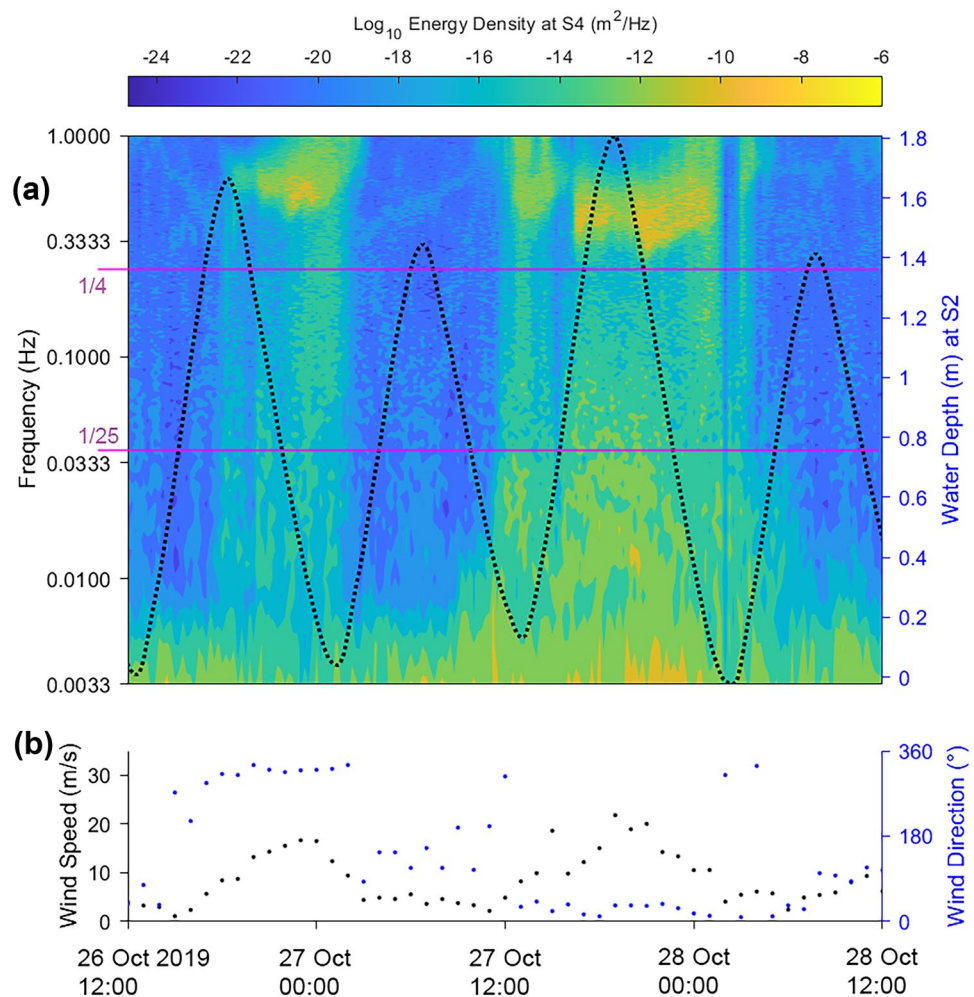
focus on it for our analysis further in this paper. We also found that sites S3 and S4, with virtually exclusively wind-frequency waves, had nearly identical timeseries in wave heights, with the exception that $H_{S,wind}$ values at S3 were approximately $\frac{1}{3}$ of values found at S4.

Thus, for simplicity and sake of comparison across sites with potential exposure to both ocean-originating and locally generated waves, we focus on data from S2 (Seal Beach) as representative of ocean-wave-influenced beaches near the mouth of Tomales Bay, and on data from S4 to represent wind-dominated beaches further landward.

The S2 site in outer Tomales Bay was regularly exposed to waves with frequencies less than $0.25Hz$ and the spectra often exhibited broad peaks around swell-range frequencies (e.g., 0.06 Hz and 0.1 Hz) with no peak at higher frequencies (see an example of a day with swell in Fig. 3). In contrast, the S4 site in inner Tomales Bay exhibited a unimodal wind-wave spectrum, with peak between 0.3 and 0.6 Hz (centered at 0.4 Hz), also visible through a representative day in Fig. 3. This spectral peak was often an order-of-magnitude higher than those observed at S2.
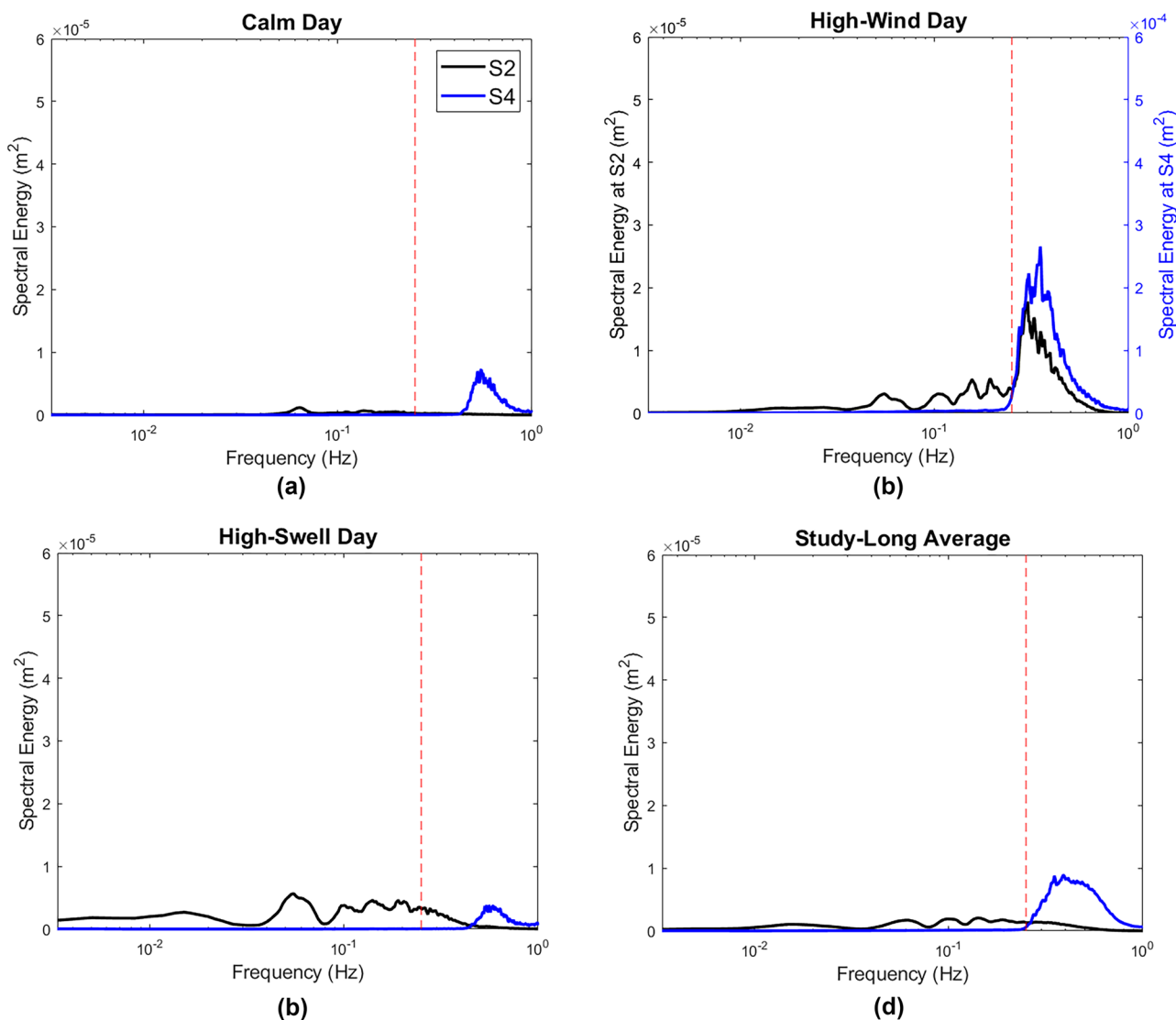
Fig. 3 Spectral averages over 24-h periods with characteristically calm conditions (**a**), windy conditions (**b**), and high offshore swell (**c**), plus study-long average spectral curves in (**d**). Note different y-axis scales in (**b**), reflecting an order-of-magnitude more wind-wave energy at S4 versus S2. Red dashed line indicates the cutoff between wind- and swell-frequency regions, 0.25 Hz

Temporal Variability in Wave Field

The modal wave conditions described above were punctuated by high-energy events owing to swell arriving at the mouth or by wind events that generated both regional wind waves outside the mouth and local wind waves inside the Bay. Figure 3 shows characteristic Wave spectra for calm conditions (October 12; Fig. 3a), windy conditions (> 20 m/s, September 28–29; Fig. 3b), and big-swell conditions ($H_S > 2$ m at offshore buoy, November 15–16; Fig. 3c). On other days with both high winds and big swell, wave spectra were a combination of those from big-wind and big-swell days. During calm conditions (October 12), wave energy was low across all frequencies at both S2 and S4 (Fig. 3a), with a weak swell peak at S2 centered at 0.064 Hz (aligned with the lowest-frequency component of an arriving swell from 318°) and a weak wind-wave peak at S4 centered at 0.55 Hz.

Outside of storm events, prevailing northwesterly winds in Tomales Bay exhibit diurnal variability, frequently reaching speeds over 8 m/s in the afternoon and early evening. We expect this pattern to drive local wave development and impact energy patterns at our sensors, especially at S3 and S4. However, $H_{S,\mathrm{wind}}$ values were strongly affected by the semi-diurnal tidal cycle as well. Our results in "Tidal Modulation of Wave Field" and discussion in "Tidal Controls on the Wave Field" makes use of our long study period to pull apart these effects and their potential phasing.

Starting at noon on September 28, winds > 20 m/s were sustained over a tidal cycle (Fig. 4). At the peak of this event, $H_{S,\mathrm{wind}}$ values at S2 and S4 were maximum for our study period, 2.5 cm and 8.2 cm, respectively. The wind-wave spectral peak averaged over an entire tidal cycle at S2 was centered around 0.45 Hz with peak energy of $3 * 10^{-5} m^2$ whereas at S4 the peak was centered at 0.33 Hz and peak energy is $5.5 * 10^{-4} m^2$. The two other wind events with high winds sustained over tidal cycles (October 4, November 19) exhibited high-frequency peaks with similar differences between S2 and S4: in general, the wind-wave spectral peak at S4 was 0.07 Hz lower in frequency and an order-of-magnitude greater in energy density than that at S2.

Spectral peaks in swell- and infragravity-frequency ranges at S1 and S2 corresponded with high H_S and T_p values at the offshore buoy. On November 15 the wind was weak, but significant swell was recorded at the offshore buoy (wave height 2.5 m, period 16 s, or 0.063 Hz), resulting in low-frequency spectral peaks at S2, centered at 0.0615 Hz, 0.0993 Hz, and 0.1434 Hz (Fig. 3c). However, at site S4 in the inner bay, a weak wind-wave peak was observed and the wave field was similar to that of a calm day (Fig. 3a). The spectral peaks at S2 represent swell and infragravity-wave periods, and similar peaks are also evident in the average spectrum at S2 (Fig. 3d).

Throughout our study period, swell and infragravity energy were observed at S1 and S2 (near-mouth "outer bay" sites)

but energy values in these ranges were negligibly small at S3 or S4 (far from the mouth, "inner bay" sites), as can be compared by the black (outer bay) and blue (inner bay) lines for example time periods if Fig. 3. Further, near-zero swell wave energy was recorded by a sensor deployed between S2 and S3 during a short summer deployment (Wall Beach, 7.0 km from Tomales Point). Swell and infragravity waves at S2 were small ($H_S < 2.5$ cm), but strongest when offshore ocean waves exhibited dominant direction from 285 to 315° N, with height $H_{S,\mathrm{buoy}}$ between 3–4 m and 13.5–16 s as the dominant period. The inner/outer bay distinction is discussed in ""Inner" vs "Outer" Bay Distinction by Wave Climate".

Swell energy arriving at our sensors varied strongly on tidal time scales (fluctuations visible in Fig. 4), generally reduced at low water levels. The peaks in $H_{S,\mathrm{swell}}$ coincident with high tides trace a falling curve shape that reflects the offshore H_S, rising to a peak on September 28 (concurrent with regional winds) and then falling through October 2. $H_{S,\mathrm{IGW}}$ demonstrates a similar but muted signal. Tidal controls are further explored in "Tidal Modulation of Wave Field", "Tidal Controls on the Wave Field", and "Lower-Frequency Wave Dynamics".

Tidal Modulation of Wave Field

In addition to fluctuations in wave sources, wave energy at our sensors in Tomales Bay varied significantly by tidal conditions. Spectra calculated for different tidal states during wave-generating conditions (both high-swell $H_S > 3$ m and high-wind speed > 10 m/s) show highest swell wave energy at S2 during high tides, and lowest energy during ebb and low tides (Fig. 5). However, the high-frequency wind waves at both S2 and S4 show highest energy during ebb tides, notably higher than flood-tide energy at the same water depth. This effect is more prevalent at S4 for wave frequencies > 0.3 Hz (Fig. 5b), although our data show similar tidal ranges at S2 and S4.

For the average low-slack and flood conditions in Fig. 5b, the spectral peak at S4 reduced in magnitude and width, and its center moved higher in frequency to near 0.54 Hz. At high slack, the spectral peak shifted to lower frequencies, with a center at 0.35 Hz. For both sensors (Fig. 5a and b), near-zero variance was observed at high slack for frequencies greater than 0.78 Hz. This is the cutoff frequency (Eq. 2) at a depth of 1.3 m. The sensors were deeper than 1.3 m for 52% of the high-tide bins, so we attribute this drop in energy to the sensor's inability to pick up high-frequency waves at high tide. This may mean our $H_{S,\mathrm{wind}}$ values are artificially low. However, if we assume that the energy values above 0.78 Hz are comparable to their average across other tidal conditions, they would only contribute only < 2% to the total energy in the wind band, both during normal and windy/swelly conditions.
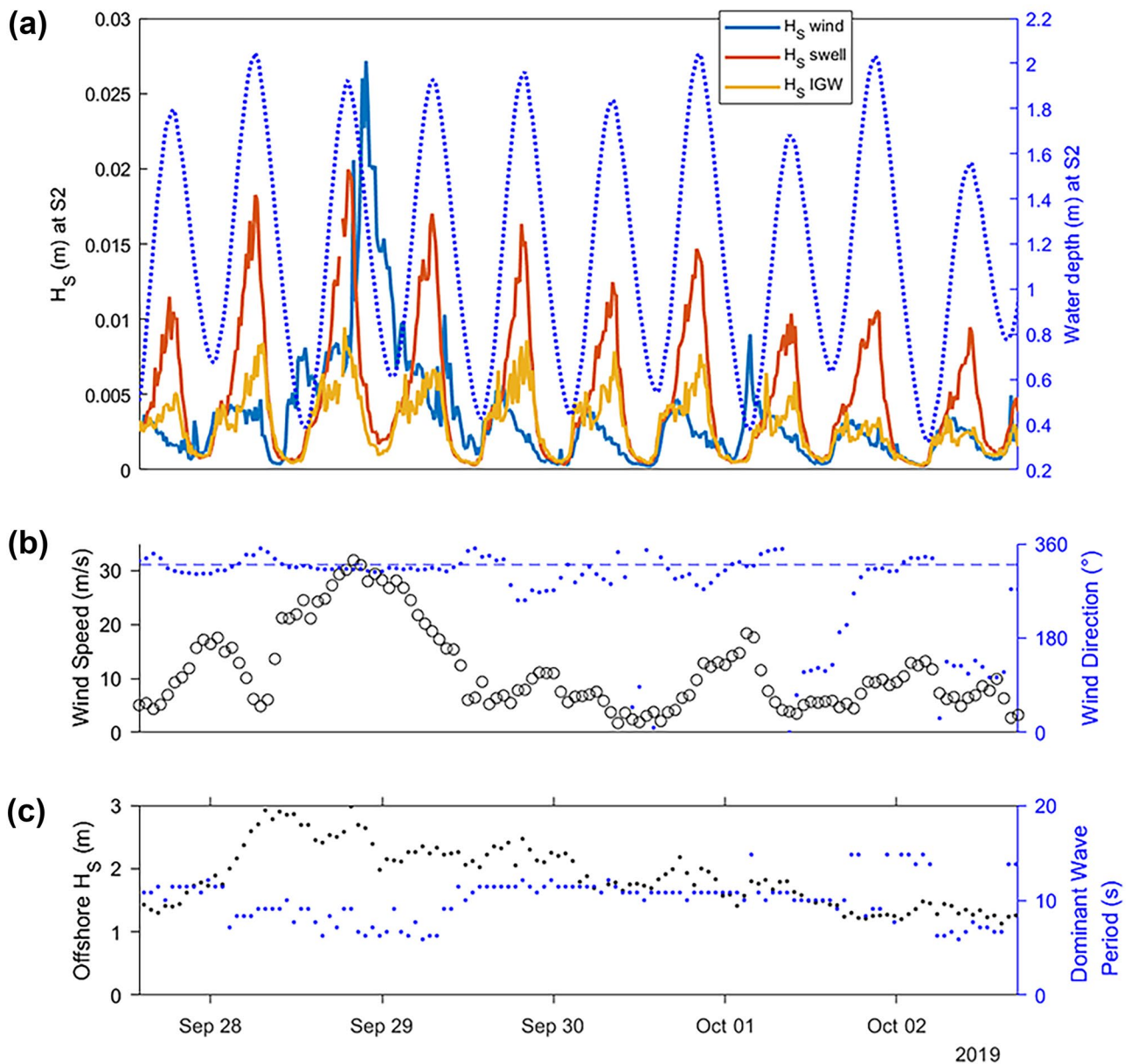
Fig. 4 High-energy events in both swell and winds co-occurred in late September 2019, demonstrating the extent of control by water level on waves of different frequencies. During this period, the dominant offshore wave direction was between 300 and 320°. The major axis of Tomales Bay, 320°, is demonstrated by the dashed blue line in (**b**)

Wave height values calculated from the tidally categorized average spectra (Fig. 5) are presented in Table 3. Broadly, wave heights (both in wind-wave band and swell band) were larger during high-slack conditions than low-slack conditions, but flooding versus ebbing affected $H_{S,wind}$ and $H_{S,swell}$ values differently. Higher $H_{S,wind}$ values were observed during ebb tides at S2 and S4, relative to other tidal conditions. However, lower $H_{S,swell}$ values were observed during ebb tides than flood tides at S2. These results are explored in "Tidal Controls on the Wave Field".

Sediment Size and Sediment Entrainment by Waves

The average D_{50} of the three beaches near S1, S2, and S3 were 0.21, 0.29, and 0.63 mm with $D_{84} - D_{16}$ spread values of 0.10, 0.24, and 2.5 mm, respectively. Grain size distributions at these four sites were unimodal with peaks in the sand range (0.062 - 2 mm). Some distributions were pure sand while the S3 samples had tails in the grain size distribution with fine-to-coarse pebble contributions (reflected by the larger spread metric). Although no sediment was collected at the beach

Fig. 5 Average spectra of four tidal condition categories across all ensembles where wind speeds were > 10 m/s and offshore H_S > 3 m, both from 280 to 340° N. (Similar spectral shapes were observed during a 20-h period on October 9, 2019, which had the requisite conditions.) Note different y-axis scales on (**a**) and (**b**). Red dashed line indicates the cutoff between wind- and swell-frequency regions, 0.25 Hz
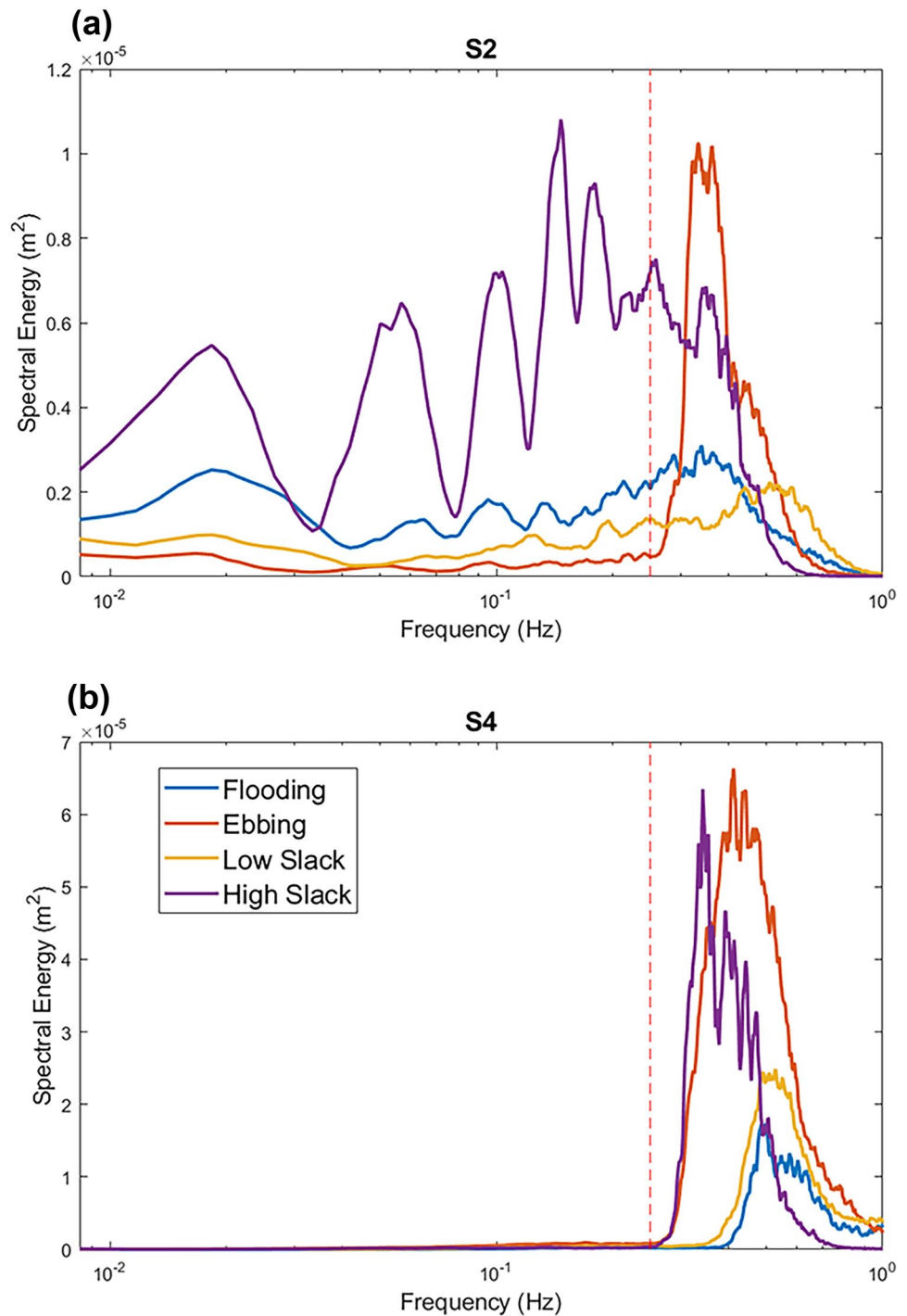
corresponding to S4, on field visits we observed the composition to be highly mixed with mud, sand, and pebble-size grains.

We considered grain entrainment as an indicator of activation (building or erosion) of the beach, in contrast to a static relic morphology. The τ_b values via Eq. 8 at S4 reached peaks of 0.18 Pa, typically at times with lower water levels (< 0.6 m water depth at the sensor) and high winds (> 10 m/s), where wind waves contributed over 70%

of the total energy. During calm-wind periods bed stress values were low with peaks of $\tau_b \approx 0.05$ Pa that occurred only at very low water levels. Background conditions between peaks had τ_b values near 0.01 Pa. These bed stress values of 0.18, 0.05, and 0.01 Pa would cross the critical τ_* (Eq. 9) threshold of 0.047 for grain sizes of 0.24 mm, 0.067 mm, and 0.013 mm respectively, all within a fine sand-to-silt range.

Table 3 Wave heights derived from the average spectra of tidal categories, during ensembles with high winds and offshore swell

Tidal Condition	No. of Ensembles	S2 $H_{S,\text{swell}}$ (cm)	S2 $H_{S,\text{wind}}$ (cm)	S4 $H_{S,\text{wind}}$ (cm)
High Slack	30	1.29	0.76	1.82
Ebbing	52	0.28	0.80	2.29
Low Slack	90	0.44	0.52	1.38
Flooding	49	0.64	0.56	1.03

In contrast, τ_b values at S2 reached peaks value of only 0.035 Pa, only 19% of the peak values of S4. These bed stresses would initiate motion of an 0.05 mm-diameter particle (coarse silt) at the sensor. Peak values of bed shear stress at S2 were typically at higher water levels (> 1.6 m at the sensor) when H_S values at the offshore buoy were > 2 m. Based on the $D_{50} = 0.29$ mm value from the beach behind S2, τ_* values (from Eq. 9) never crossed the critical τ_* value during our study period, with τ_* peaking at values near 0.01.

Discussion

Dynamics of the Wave Field

Wind-Wave Dynamics

Local winds have the potential to develop waves anywhere in the bay, and the largest high-frequency energy levels observed were at the site with the longest in-bay fetch—S4. In Fig. 3b it is evident that the spectral energy values at S4 are an order-of-magnitude greater than at S2, and, as mentioned in "Overview of Observed Wave Field'', a factor of 3 greater than at S3. Wave heights with wind-wave frequencies (> 0.25 Hz) differed by tidal conditions (the last two columns of Table 3) after controlling for wind speeds, suggesting tidal effects on the generation or attenuation mechanisms of these waves. The larger relative changes by tidal category, larger absolute $H_{S,\text{wind}}$ values (and energy magnitudes), and lower-frequency T_p values at S4 than S2 (as mentioned in "Temporal Variability in Wave Field'') are attributable to the much longer fetch at S4 than S2, with longer cumulative distance for both wave development and attenuation processes to manifest.

Larger waves at higher tides cannot be explained by longer fetch at high water (as in Fagherazzi and Wiberg (2009)) due to the nature of Tomales Bay. While at high tide open water extends over 17.4 km from the mouth of the bay to S4, at low tide the fetch is effectively reduced by the Walker Creek tidal delta and shoals along the eastern side of the bay, down to as low as approximately 10 km. S2, by its placement near the deep channel, has its fetch confined to the deep channel at low

tide, approximately a kilometer. In addition to tidal variation in wave generation, depth-controlled variation in bottom friction and currents may influence wave attenuation (Davidson et al. 2008)—see "Tidal Controls on the Wave Field".

Wind wave heights predicted using equations from Young and Verhagen (1996) at S4 were much lower than those from our data; we observed maximum H_S values at S4 of 0.09 m (at high tide) and 0.06 m (at low tide) during hours of > 25 m/s winds centered around 22:00 on September 28th, whereas the intermediate-depth prediction of Young and Verhagen (1996) was 0.013 m (at either tidal stage). In contrast, the Coastal Engineering Research Center (1984), which has empirical formulas (3-33 and 3-34) for fetch-limited wave development but in deep water, predicts a wave height of 2.5 m at S4 for these conditions. At S2, the pattern is the same: the maximum observed H_S during these conditions was 0.033 m, but what was predicted by Young and Verhagen (1996) was 0.007 m. Again, the Coastal Engineering Research Center (1984) overpredicts with 1.1 m. Some of this discrepancy may be explained by the geographic location of our 10 m wind speed data, outside of Tomales Bay at BML, although waves over 0.5 m are very rare in Tomales Bay (David Dann, personal communication). The bathymetry of the outer bay is shallow, with a deep channel intersecting tidal shoals between the mouth and Hog Island (Fig. 1), making it difficult to choose single depth and fetch values to use these wave prediction formulas, especially for locations deep inside the bay. Additionally unaddressed are shoaling processes near our sensor locations: (i) waves may shoal in shallow water, accounting for wave heights greater than offshore, and (ii) offshore of the sensor location extensive mudflats can dissipate significant wave energy before waves are quantified at sensor locations, accounting for wave heights lower than offshore. This second effect may be exacerbated by aquatic vegetation, like eelgrass beds. Both processes require more attention to properly quantify their effect.

Lower-Frequency Wave Dynamics

Our findings suggest that swell and infragravity waves are not present at our sensor sites 8.0 km and further from the mouth of the bay at Tomales Point. Swell and infragravity energy observed at S2 partially followed the height and period of offshore waves observed at the offshore buoy. Oceanic swell has been observed on mudflat-fronted shorelines in nearby San Francisco Bay, similarly correlated with offshore wave energy by Talke and Stacey (2003), and at beaches some kilometers from the mouth of Botany Bay, Australia by Rahbani et al. (2022). Hughes et al. (2014) point to a linear relationship between energy levels from swell and IGW versus deep water wave height, but in our study there was only a rough relationship. While the 1 m "baseline" H_S values at the offshore buoy were sufficient to

register swell-frequency fluctuations at S2 (see falling H_S in Fig. 4), much of the variation in $H_{S,\text{swell}}$ is controlled by tidal patterns, as further discussed in "Tidal Controls on the Wave Field".

"Inner" vs "Outer" Bay Distinction by Wave Climate

The outer bay coastline is influenced more by regular swell waves during high-tide periods, and lacks enough fetch for local winds to drive larger wind chop. This is in contrast to inner bay sites that may receive no swell waves but that are more exposed to high-energy wind-wave events when local winds are strong. That said, the distance between the sensor and the beach is critical to link nearshore wave conditions to beaches. In our study, S4 was 100 m from the beach due to a low-slope fronting mudflat—this is discussed more in "Beach-Shaping Implications". Given the characteristic differences discussed in "Overview of Observed Wave Field", data from S2 serves as a template of a sand-dominated near-channel beach in the Bay, and is close enough to the mouth to be influenced by swell—an "outer bay" beach. Data from S4, on the other hand, represents a mudflat-fronted beach far inside the Bay, where effects of swell are absent; at these "inner bay" beaches, wave energy is due to locally generated wind waves. Further, differences in the tidally varying wave signal are observed owing to differences in bathymetry and dominant wave period at inner- and outer-bay sites. This inner/outer distinction in Tomales Bay is supported by hydrodynamic modeling by Gross and Stacey (2004) and sedimentation patterns detailed by Rooney and Smith (1999) and can be expected to be observed in other semi-enclosed bays where ocean waves are absent from an "inner bay" region.

Tidal Controls on the Wave Field

Tidal conditions affected the amount of energy within different energy bands in different ways, as evident in Table 3 and in averages of spectra from different tidal conditions in Fig. 5.

Tidal currents are known to modify spectral distributions and wave energy (e.g., Huang et al. (1972); Dodet et al. (2013)), especially in bays where ebbing currents may "block" swell and infragravity waves from entering the inlet (Chen et al. (1998) and Bertin et al. (2018)). Tidal currents in Tomales Bay reach a maximum of about 1 m/s in the channels of the outer bay (Gross and Stacey 2004). During maximum ebb tide currents, waves with group celerity less than 1 m/s may not be able to enter Tomales Bay— however, this celerity corresponds with waves with frequency above 0.78 Hz (1.28 s) as solved using Eqs. 5 and 6 using 11 m as a reference depth of the mouth of Tomales Bay (Anima et al. 2008). This value is close to our Nyquist limit, and the spectral energy attributable to frequencies higher than this less than $10^{-6} m^2$ for all sites in the average conditions during the deployment. Thus, at most, wave-blocking at the mouth may preclude extremely high-frequency wind waves from entering the Bay, which are expected to make small contributions to the total wave energy, especially at sites close to the mouth which are more swell-dominated.

Also, tidal currents may affect waves in other ways, e.g., flood-tide currents will speed the propagation of ocean-generated waves into the bay, shortening the travel time and effective propagation distance, resulting in reduced attenuation. This is consistent with our observations of greater swell and IGW energy during flood and high tides at S2. In our study, ebbing tidal conditions carried amplified high-frequency spectral energies across the entire embayment, evident in $H_{S,\text{wind}}$ values in Table 3. This effect may be due to wave steepening by opposing currents (Dodet et al. 2013). The effects of flooding on wind-frequency waves were slightly different at S2 and S4, with flooding conditions carrying a 27% decrease in $H_{S,\text{wind}}$ relative to low-slack tide conditions—also a pattern suggested by Dodet et al. (2013)—but a small 8% increase at S2, a pattern evident in Fig. 5. However, tidal currents in the inner bay are known to be small (0.2 m/s, Gross and Stacey (2004)) and the effect may be more easily explained by differences in wind-wave generation patterns in the following paragraph.

During periods with exceptionally high winds—e.g., the peak of nearly 30 m/s winds very late on September 28 and the smaller but prominent peak of nearly 20 m/s winds early on October 1 (Fig. 4) — the wave field remains or becomes excited above near-zero conditions despite low water levels at S2 (Fig. 4). The same effect was observed at S4. The observed capacity for the wind wave field to remain excited through low water levels introduces the possibility of tidally controlled hysteresis in the wave field during windy conditions (Fig. 6a). In this conceptualization, high water levels with less bottom friction allow the sea state to develop in response to the winds, with increasing $H_{S,\text{wind}}$ and T_p values. Then, during ebbing conditions, the sea may continue to saturate while wave attenuation processes begin to exert stronger control as the water depth decreases later on the ebb tide. In contrast, as flooding conditions begin, the wave field is developing from a low-energy state and lower wind-wave energy can be expected on flood tides for the same water depth compared with ebb tides. This tidal trajectory would explain the higher $H_{S,\text{wind}}$ value during ebbing conditions at S2 and S4.

In contrast, the outer bay (i.e., swell-receiving) sites have a different hysteresis pattern with water depth and $H_{S,\text{swell}}$, conceptually illustrated in Fig. 6b. The lower-frequency waves are not dependent on tidal conditions for generation, but their attenuation does depend on tidal conditions as outlined above, thus reversing their trajectory through wave height-water depth space: swell (and IGW) energies were reduced during ebb and low tides at S2 relative to other tidal conditions (Fig. 5 and Table 3). During ebbing conditions, $H_{S,\text{swell}}$ may be strongly attenuated due to decreasing water depths and opposing currents in the outer bay, with wave energy falling lower
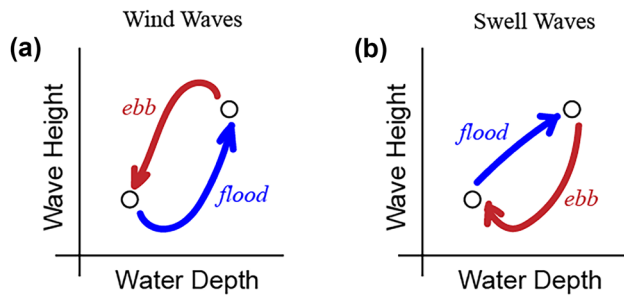
Fig. 6 Conceptual diagram of wave height modulation by tidal conditions for wind-frequency energy (**a**) and swell-frequency energy (**b**). While the pattern in (**a**) may be present anywhere in an embayment, the pattern in (**b**) will only be present at outer bay sites that receive swell

even than during low-slack conditions. Then, as water levels rise, the converse happens. Additional studies are required to provide more quantitative understanding of tidal controls and specifically wave-current interaction.

Beach-Shaping Implications

While our sensors were placed with some distance from the shoreline (28 m for S2, 104 m for S4), the wave energies observed may have implications for beach morphologic change. At both S2 and S4, beach-building conditions are most likely to occur at high tide, because of the highest available wave energy reaching the beach, as in Trindade et al. (2016) where shoals/bars prevented waves from reaching beaches during lower water levels. For the outer-bay beach (S2), high water levels permit more swell to enter the bay and impact the beach. For the inner-bay beach (S4), high water levels permit larger wave generation, but early ebbing conditions may raise wave energy. During lower water levels at S4, the short, shallow wind waves are likely attenuated by the mudflats and subtidal vegetation, as found in San Francisco Bay by Lacy and MacVean (2016).

During our study period, the observed waves were too small to move their respective $D50$-sized particles ("Sediment Size & Sediment Entrainment by Waves"), rendering the beaches morphologically inactive. As our study period captured a typical sea breeze, this suggests the summer and fall seasons—when sea breeze is present and NW swells are smaller than winter/spring—are periods of little beach change. The BEBs in Tomales Bay likely have relict morphologies created by prior high-energy events from local storms or especially high winter swells from the NW, for the outer bay sites. Morphologies determined by prior high-energy events on decadal timescales are common among BEBs and have been reported by authors including Costas et al. (2005), Fellowes et al. (2021), and Gallop et al. (2020). If different particle sizes can be resuspended independently,

then fine sediment may have been resuspended during wave conditions observed in this study, but it is outside this study to address very low-lying or subtidal fine sediment features. Visual observations of near-beach turbidity corroborate this winnowing phenomenon, but these fines do not contribute to beach building.

Sediment availability and the general geologic context also serve as strong controls on beach location and morphology (Gallop et al. 2020). Broadly, Tomales Bay acts as a littoral-cell adjacent system of shoals with fluvial input from Walker Creek near the mouth and marine sediments extending as far as Hog Island (Johnson and Beeson 2019); a deep sink in the central bay; and a second sediment supply via the Lagunitas Creek delta at the southern end of the Bay (Rooney and Smith 1999). For beaches in central Tomales Bay, with no connection to the flood-tide or fluvial deltas, and only very small adjacent watersheds, available sediment may be limited to local input (i.e., shoreline erosion). The beach at Tomasini Point (S4) exhibits a high incidence of coarse pebbles, and may be undergoing winnowing during even mild winds at high tides (wind waves resuspend fines that are transported away by tidal currents). Some replacement of the fines may occur during floods or due to fluvial inputs, but resolving this question and others around sediment provenance requires additional work outside the scope of this study. Future work could illuminate the combination of factors and timescales of active beach morphologic change, but our paper supports that the high-energy events of our study period were not enough to activate the relic beaches, and that, in any season, co-occurence of swell or wind events with high and ebbing tides (respectively) yield the greatest likelihoods of wave energies to drive beach evolution.

Conclusions

In this study, we used wind- and swell-band spectral energy values to identify patterns in the responses to forcings in the wave field at four near-beach sites in Tomales Bay, California. Sites near the mouth received swell waves that correlated with the wave climate offshore. All sites received wind waves during windy periods, with larger wind waves observed deeper inside the bay, bringing attention to in-bay wave-generating mechanisms. The dominance of different frequency bands can be used to distinguish between two categories of site: those dominated by remote waves and lacking fetch to receive large winds from local winds—near-mouth "outer bay" sites—and those without swell, dominated by local wind waves—"inner bay" sites. Wave energy values of both types were modulated by tidal conditions after controlling for wave-generating mechanisms, with high water levels permitting more swell energy to reach the outer bay sites and more development of the local wind wave field. Observed

in-bay wave heights were small throughout the bay, and no events that could transport bottom sediments at our sensors were recorded, suggesting the beaches are morphologically inactive during time periods such as our deployment. Our study addresses literature gaps around spectral data in sheltered waters and highlights the value in segmenting spectral energy to understand the dynamics of embayed wave fields. We point to the necessity for further study into wave-tide interactions in fetch- and/or depth-limited contexts.

References

Anima, R.J., J.L. Chin, D.P. Finlayson, M.L. McGann, and F.L. Wong. 2008. *Interferometric Sidescan Bathymetry*. California: Sediment and Foraminiferal Analyses; a New Look at Tomales Bay.

Beach, R.A., and R.W. Sternberg. 1992. Suspended sediment transport in the surf zone: Response to incident wave and longshore current interaction. *Marine Geology*. 108 (3–4): 275–294.

Bertin, X., A. de Bakker, A. van Dongeren, G. Coco, G. André, F. Ardhuin, P. Bonneton, F. Bouchette, B. Castelle, W.C. Crawford, M. Davidson, M. Deen, G. Dodet, T. Guérin, K. Inch, F. Leckler, R. McCall, H. Muller, M. Olabarrieta, D. Roelvink, et al. 2018. Infragravity waves: From driving mechanisms to impacts. *Earth-Science Reviews*. 177: 774–799.

Bishop, C.T., and M.A. Donelan. 1987. Measuring waves with pressure transducers. *Coastal Engineering*. 11 (4): 309–328.

Chen, Q., P.A. Madsen, H.A., Schäffer, and D.R. Basco. 1998. Wave-current interaction based on an enhanced Boussinesq approach. *Coastal Engineering*. 33 (1): 11–39. https://doi.org/10.1016/S0378-3839(97)00034-3. https://linkinghub.elsevier.com/retrieve/pii/S0378383997000343.

Coastal Engineering Research Center. 1984. *Shore Protection Manual*, vol. 1.

Costas, S., I., Alejo, A., Vila-Concejo, and M.A. Nombela. 2005. Persistence of storm-induced morphology on a modal low-energy beach: A case study from NW-Iberian Peninsula. *Marine Geology*. 224 (1–4): 43–56. https://doi.org/10.1016/j.margeo.2005.08.003. https://linkinghub.elsevier.com/retrieve/pii/S0025322705002641.

Davidson, M.A., T.J. O'Hare, and K.J. George. 2008. Tidal modulation of incident wave heights: Fact or fiction? *Journal of Coastal Research*. 24 (2B): 151–159. https://doi.org/10.2112/06-0754.1. http://www.bioone.org/doi/abs/10.2112/06-0754.1.

Dodet, G., X. Bertin, N. Bruneau, A.B. Fortunato, A. Nahon, and A. Roland. 2013. Wave-current interactions in a wave-dominated tidal inlet. *Journal of Geophysical Research: Oceans*. 118 (3): 1587–1605. https://doi.org/10.1002/jgrc.20146. http://doi.wiley.com/10.1002/jgrc.20146.

Eliot, M.J., A. Travers, and I. Eliot. 2006. Morphology of a Low-energy beach, Como Beach, Western Australia. *Journal of Coastal Research*. 221: 63–77. https://doi.org/10.2112/05A-0006.1. http://www.bioone.org/doi/abs/10.2112/05A-0006.1.

Ellis, J.T., D.J. Sherman, and B.O. Bauer. 2006. Depth compensation for pressure transducer measurements of boat wakes. *Journal of Coastal Research*. 1 (39): 6.

Fagherazzi, S., and Wiberg PL. 2009. Importance of wind conditions, fetch, and water levels on wave-generated shear stresses in shallow intertidal basins. *Journal of Geophysical Research*. 114 (F3): F03022. https://doi.org/10.1029/2008JF001139. http://doi.wiley.com/10.1029/2008JF001139.

Fellowes, T.E., A. Vila-Concejo, S.L. Gallop, R. Schosberg, V. de Staercke, and J.L. Largier. 2021. Decadal shoreline erosion and recovery of beaches in modified and natural estuaries. *Geomorphology*. 390: 107884. https://doi.org/10.1016/j.geomorph.2021.107884. https://www.sciencedirect.com/science/article/pii/S0169555X21002920.

Foster-Martinez, M.R., J.R. Lacy, M.C. Ferner, and E.A. Variano. 2018. Wave attenuation across a tidal marsh in San Francisco Bay. *Coastal Engineering*. 136: 26–40. https://doi.org/10.1016/j.coastaleng.2018.02.001. https://linkinghub.elsevier.com/retrieve/pii/S0378383917305525.

Gallop, S.L., D.M. Kennedy, C. Loureiro, L.A. Naylor, J.J. Muñoz-Pérez, D.W.T. Jackson, and T.E. Fellowes. 2020. Geologically controlled sandy beaches: Their geomorphology, morphodynamics and classification. *Science of The Total Environment*. 731: 139123. https://doi.org/10.1016/j.scitotenv.2020.139123. https://linkinghub.elsevier.com/retrieve/pii/S0048969720326401.

Gross, E.S., and M.T. Stacey. 2004. Three-Dimensional Hydrodynamic Modeling of Tomales Bay, California. In *Estuarine and Coastal Modeling (2003)*, 646–666. Monterey, California, United States: American Society of Civil Engineers. https://doi.org/10.1061/40734(145)40. http://ascelibrary.org/doi/10.1061/40734%28145%2940.

Huang, N.E., D.T. Chen, and C.C. Tung. 1972. Interactions between steady non-uniform currents and gravity waves with applications for current measurements. *Journal of Physical Oceanography*. 2: 420–431.

Hughes, M.G., T. Aagaard, T.E. Baldock, and H.E. Power. 2014. Spectral signatures for swash on reflective, intermediate and dissipative beaches. *Marine Geology*. 355: 88–97. https://doi.org/10.1016/j.margeo.2014.05.015. https://linkinghub.elsevier.com/retrieve/pii/S0025322714001492.

Jackson, N.L., K.F. Nordstrom, I. Eliot, and G. Masselink. 2002. 'Low energy' sandy beaches in marine and estuarine environments: A review. *Geomorphology*. 48 (1–3): 147–162. https://doi.org/10.1016/S0169-555X(02)00179-4. https://linkinghub.elsevier.com/retrieve/pii/S0169555X02001794.

Johnson, S.Y., and J.W. Beeson. 2019. Shallow structure and geomorphology along the offshore Northern San Andreas Fault, Tomales Point to Fort Ross, California. *Bulletin of the Seismological Society of America*. 109 (3): 833–854. https://doi.org/10.1785/0120180158. https://pubs.geoscienceworld.org/ssa/bssa/article/109/3/833/569714/Shallow-Structure-and-Geomorphology-along-the.

Jones, N.L., and S.G. Monismith. 2007. Measuring short-period wind waves in a tidally forced environment with a subsurface pressure

gauge: Measuring waves with pressure gauges. *Limnology and Oceanography: Methods*. 5 (10): 317–327. https://doi.org/10.4319/lom.2007.5.317. http://doi.wiley.com/10.4319/lom.2007.5.317.

Lacy, J.R., and L.J. MacVean. 2016. Wave attenuation in the shallows of San Francisco Bay. *Coastal Engineering*. 114: 159–168. https://doi.org/10.1016/j.coastaleng.2016.03.008. https://linkinghub.elsevier.com/retrieve/pii/S0378383916300369.

Leonardi, N., N.K. Ganju, and S. Fagherazzi. 2016. A linear relationship between wave power and erosion determines salt-marsh resilience to violent storms and hurricanes. *Proceedings of the National Academy of Sciences*. 113 (1): 64–68. https://doi.org/10.1073/pnas.1510095112. http://www.pnas.org/lookup/doi/10.1073/pnas.1510095112.

Madsen, O.S., and W.D. Grant. 1975. The Threshold of Sediment Movement Under Oscillatory Waves: A Discussion. *Journal of Sedimentary Petrology*. 45: 360–361.

Marani, M., A. D'Alpaos, S. Lanzoni, and M. Santalucia. 2011. Understanding and predicting wave erosion of marsh edges. *Geophysical Research Letters*. 5.

Matsuba, Y., T. Shimozono, and Y. Tajima. 2021. Tidal modulation of infragravity wave dynamics on a reflective barred beach. *Estuarine, Coastal and Shelf Science*. 261: 107562. https://doi.org/10.1016/j.ecss.2021.107562. https://linkinghub.elsevier.com/retrieve/pii/S0272771421004121.

McPhee-Shaw, E E., K.J. Nielsen, J.L. Largier, and B.A. Menge. 2011. Nearshore chlorophyll-a events and wave-driven transport. *Geophysical Research Letters*, *38*(2). https://doi.org/10.1029/2010GL045810.

Millero, F.J., C.T. Chen, A. Bradshaw, and K. Schleicher. 1980. A new high pressure equation of state for seawater. *Deep-Sea Research*. 27A: 255–264.

NDBC. 2020. NDBC - Station 46013 Recent Data. National Buoy Data Center. https://www.ndbc.noaa.gov/station_page.php?station=46013. Accessed 15 Apr 2020.

Nielsen, P. 1992. Coastal bottom boundary layers and sediment transport, vol. 4 of Advanced Series on Ocean Engineering. *World Scientific*. https://doi.org/10.1142/1269. https://www.worldscientific.com/worldscibooks/10.1142/1269.

NOAA. 2020. 9415020, Point Reyes CA | Datums - NOAA Tides & Currents. National Oceanic and Atmospheric Administration. https://tidesandcurrents.noaa.gov/datums.html?datum=MLLW &units=1 &epoch=0 &id=9415020 &name=Point+Reyes &state=CA. Accessed 15 Apr 2020.

Okihiro, M., and R.T. Guza. 1995. Infragravity energy modulation by tides. *Journal of Geophysical Research*. 100 (C8): 16143–16148.

Rahbani, M., A. Vila-Concejo, T.E. Fellowes, S.L. Gallop, L. Winkler-Prins, and J.L. Largier. 2022. Spatial patterns in wave signatures on beaches in estuaries and bays. *Geomorphology*. 398: 108070. https://doi.org/10.1016/j.geomorph.2021.108070. https://linkinghub.elsevier.com/retrieve/pii/S0169555X21004785.

Rooney, J.J., and S.V. Smith. 1999. Watershed Landuse and Bay Sedimentation. *Journal of Coastal Research*. 15: 8.

Talke, S.A. and M.T. Stacey. 2003. The influence of oceanic swell on flows over an estuarine intertidal mudflat in San Francisco Bay. *Estuarine, Coastal and Shelf Science*. 58 (3): 541–554. https://doi.org/10.1016/S0272-7714(03)00132-X. https://linkinghub.elsevier.com/retrieve/pii/S027277140300132X.

Trindade, W., L.C.C. Pereira, and A. Vila-Concejo. 2016. Tidal modulation of moderate wave energy on a sandy tidal flat on the macrotidal amazon littoral. *Journal of Coastal Research*. 75 (sp1): 487–491. https://doi.org/10.2112/SI75-098.1. http://www.bioone.org/doi/10.2112/SI75-098.1.

Vila-Concejo, A., S.L. Gallop, and J.L. Largier. 2020. Sandy beaches in estuaries and bays. In *Sandy Beach Morphodynamics*, ed. D.W.T. Jackson and A.D. Short, 343–362. Elsevier. https://doi.org/10.1016/B978-0-08-102927-5.00015-1 . https://www.sciencedirect.com/science/article/pii/B9780081029275000151.

Wentworth, C.K. 1922. A scale of grade and class terms for clastic sediments. *The Journal of Geology*. 30 (5): 377–392. http://www.jstor.org/stable/30063207.

Wiberg, P.L., and C.R. Sherwood. 2008. Calculating wave-generated bottom orbital velocities from surface-wave parameters. *Computers & Geosciences*. 34 (10): 1243–1262.

Williams, M.E., and M.T. Stacey. 2016. Tidally discontinuous ocean forcing in bar-built estuaries: The interaction of tides, infragravity motions, and frictional control. *Journal of Geophysical Research: Oceans*. 121 (1): 571–585. https://doi.org/10.1002/2015JC011166. https://onlinelibrary.wiley.com/doi/abs/10.1002/2015JC011166.

Young, I.R., and L.A. Verhagen. 1996. The growth of fetch limited waves in water of finite depth. Part 1. Total energy and peak frequency. *Coastal Engineering*. 29 (1-2): 47–78. https://doi.org/10.1016/S0378-3839(96)00006-3. https://linkinghub.elsevier.com/retrieve/pii/S0378383996000063.

Zhu, L., Q. Chen, H. Wang, W. Capurso, L. Niemoczynski, K. Hu, and G. Snedden. 2020. Field observations of wind waves in upper delaware bay with living shorelines. *Estuaries and Coasts*. 43 (4): 739–755. https://doi.org/10.1007/s12237-019-00670-7. http://link.springer.com/10.1007/s12237-019-00670-7.